Medical Physics
The International Journal of Medical Physics Research and Practice

A GPU based high-resolution multilevel biomechanical head and neck model for validating deformable image registration

J. Neylon, X. Qi, K. Sheng, R. Staton, J. Pukala, R. Manon, D. A. Low, P. Kupelian, and A. Santhanam

Citation: Medical Physics **42**, 232 (2015); doi: 10.1118/1.4903504
View online: http://dx.doi.org/10.1118/1.4903504
View Table of Contents: http://scitation.aip.org/content/aapm/journal/medphys/42/1?ver=pdfcov
Published by the American Association of Physicists in Medicine

A GPU based high-resolution multilevel biomechanical head and neck model for validating deformable image registration

J. Neylon,[a] X. Qi, and K. Sheng
Department of Radiation Oncology, University of California Los Angeles, 200 Medical Plaza, #B265, Los Angeles, California 90095

R. Staton, J. Pukala, and R. Manon
Department of Radiation Oncology, M.D. Anderson Cancer Center, Orlando, 1440 South Orange Avenue, Orlando, Florida 32808

D. A. Low, P. Kupelian, and A. Santhanam
Department of Radiation Oncology, University of California Los Angeles, 200 Medical Plaza, #B265, Los Angeles, California 90095

(Received 12 June 2014; revised 17 November 2014; accepted for publication 18 November 2014; published 22 December 2014)

Purpose: Validating the usage of deformable image registration (DIR) for daily patient positioning is critical for adaptive radiotherapy (RT) applications pertaining to head and neck (HN) radiotherapy. The authors present a methodology for generating biomechanically realistic ground-truth data for validating DIR algorithms for HN anatomy by (a) developing a high-resolution deformable biomechanical HN model from a planning CT, (b) simulating deformations for a range of interfraction posture changes and physiological regression, and (c) generating subsequent CT images representing the deformed anatomy.
Methods: The biomechanical model was developed using HN kVCT datasets and the corresponding structure contours. The voxels inside a given 3D contour boundary were clustered using a graphics processing unit (GPU) based algorithm that accounted for inconsistencies and gaps in the boundary to form a volumetric structure. While the bony anatomy was modeled as rigid body, the muscle and soft tissue structures were modeled as mass–spring-damper models with elastic material properties that corresponded to the underlying contoured anatomies. Within a given muscle structure, the voxels were classified using a uniform grid and a normalized mass was assigned to each voxel based on its Hounsfield number. The soft tissue deformation for a given skeletal actuation was performed using an implicit Euler integration with each iteration split into two substeps: one for the muscle structures and the other for the remaining soft tissues. Posture changes were simulated by articulating the skeletal structure and enabling the soft structures to deform accordingly. Physiological changes representing tumor regression were simulated by reducing the target volume and enabling the surrounding soft structures to deform accordingly. Finally, the authors also discuss a new approach to generate kVCT images representing the deformed anatomy that accounts for gaps and antialiasing artifacts that may be caused by the biomechanical deformation process. Accuracy and stability of the model response were validated using ground-truth simulations representing soft tissue behavior under local and global deformations. Numerical accuracy of the HN deformations was analyzed by applying nonrigid skeletal transformations acquired from interfraction kVCT images to the model's skeletal structures and comparing the subsequent soft tissue deformations of the model with the clinical anatomy.
Results: The GPU based framework enabled the model deformation to be performed at 60 frames/s, facilitating simulations of posture changes and physiological regressions at interactive speeds. The soft tissue response was accurate with a R^2 value of >0.98 when compared to ground-truth global and local force deformation analysis. The deformation of the HN anatomy by the model agreed with the clinically observed deformations with an average correlation coefficient of 0.956. For a clinically relevant range of posture and physiological changes, the model deformations stabilized with an uncertainty of less than 0.01 mm.
Conclusions: Documenting dose delivery for HN radiotherapy is essential accounting for posture and physiological changes. The biomechanical model discussed in this paper was able to deform in real-time, allowing interactive simulations and visualization of such changes. The model would allow patient specific validations of the DIR method and has the potential to be a significant aid in adaptive radiotherapy techniques. © *2015 American Association of Physicists in Medicine.* [http://dx.doi.org/10.1118/1.4903504]

Key words: GPU, biomechanical model, deformable image registration, adaptive radiotherapy

1. INTRODUCTION

The term head and neck cancer (HNC) refers to a group of biologically similar cancers originating from the upper aerodigestive tract, including the lip, oral cavity (mouth), nasal cavity, para nasal sinuses, pharynx, and larynx. 90% of head and neck (HN) cancers are squamous cell carcinomas (SCCHN), originating from the mucosal lining (epithelium) of these regions.[1] HNC often spreads to the lymph nodes of the neck, leading to cancer metastasis in the rest of the patient's body.[2] Radiotherapy (RT) has seen a major push toward treatment plans for the HNC that are tailored to the patient and adapted to their radiation response.[3–6] Ignoring patient misalignments caused by nonrigid changes in patient posture and physiology can lead to underdosing the tumor and overirradiating the healthy tissue.[5,7] Image-guided analyses of such nonrigid head and neck anatomy variations were made possible by use of deformable image registration (DIR) frameworks that register the patient planning anatomy with the treatment anatomy. Such analyses have led to several indications on the need for better patient aligning. For instance, Wang *et al.*[8] showed that uncorrected patient positioning misalignments would increase the maximum dose to both the brainstem and spinal cord by 10 Gy and the mean dose to the left and right parotid glands by 7.8 and 8.5 Gy, respectively. Similarly, 95% of the gross tumor volume (GTV) and clinical target volume (CTV) would decrease by 4 and 5.6 Gy, respectively.

The accuracy of DIR to help quantify patient posture and physiological changes is critical for the success of adaptive RT. Adaptive RT will employ quantitative dose delivery error characterization and subsequent compensatory strategies. However, DIR development has been hampered by a lack of techniques that generate ground-truth deformations that can be used to evaluate competing DIR algorithms. This paper focuses on developing a biomechanical model that will be the first step toward generating ground-truth deformations that can be used for validating both image registration and adaptive RT frameworks. Biomechanical human anatomy models have been developed for applications ranging from computer animation to CT image registration.

Sophisticated biomechanical models have been developed for individual anatomical sites, including the head and neck,[9–12] the hand,[16–18] lungs,[19] and the leg.[21] Such models, when developed from patient CT or MRI, can create subject specific physiological and musculoskeletal dynamic atlas. As an example, subject specific cardiac models of normal and diseased heart have been developed using nonuniform rational Bezier splines (NURBS) in order to simulate the cardiac motion before and after the treatment.[20] Physics-based methods, such as finite element methods and mass–spring models, have been applied for deforming anatomy of the torso,[13–15] and the biomechanical nature of these models also allows for the inclusion of subject specific tumor representations and day-to-day variations in the treatment.

The focus of this paper is on the biomechanical head and neck model development that can be used for validating DIR algorithms for the head and neck anatomy. The human head-neck musculoskeletal system is highly complex with approximately 57 articular bones and many more muscle actuators. Comprehensive biomechanical modeling and control of the head and neck anatomy is the most principled approach for simulating subtle deformations such as neck rotation movements and physiological changes such as tumor shrinkage and internal organ movements.

To construct precise ground-truth data for validating DIR, which provides clinically realistic deformations, where the motion of each voxel is known, the biomechanical models need to satisfy the following: (a) the model must have a one-to-one correspondence with the reference anatomy, i.e., for every voxel in the reference anatomy, the model must include a model element (e.g., a node with an assigned mass and elasticity), and vice versa, (b) the model must simulate both posture as well as physiological changes, and (c) the model must be validated to ensure clinical relevance. In this paper, we present a method for deforming a high-resolution biomechanical head and neck model. In order to address the high computational demands of this method, we present algorithms to employ a graphics processing unit (GPU) based computational framework.

The key contribution of this paper is as follows: (a) to our knowledge, this is the first work to demonstrate a GPU framework for deforming a high resolution biomechanical head and neck model at interactive speeds; (b) the model anatomy maintains a one-to-one correspondence between a planning CT anatomy such that the model can compute the displacement of every voxel in the CT without employing any interpolation; and (c) the model also generates an equivalent CT data set for validating image-based registration algorithms.

2. MODEL DEVELOPMENT

2.A. Data acquisition

Images for this study were acquired as part of an IRB-approved prospective adaptive radiotherapy protocol at M.D. Anderson Cancer Center Orlando. The planning kVCTs as well as the repeated weekly kVCTs for all patients were acquired using a Philips Brilliance CT system (Philips Medical Systems, Best, the Netherlands) or a Siemens Biograph 64 PET/CT system (Siemens AG, Munich, Germany) with $1 \times 1 \times 3$ mm^3 reconstructed resolution. Soft tissue and rigid structures were manually contoured in each of the datasets using a commercial contouring tool (MimVista®, Inc., Cleveland, OH).

2.B. Structured volume generation

The contours represented the structure outlines and were transmitted as an ordered series of contour vertices. The proposed head and neck deformation algorithm required assignments of each voxel to a single structure and so a structured volume algorithm was developed to assign the voxels based on the contour vertices. The algorithm was as follows:

(1) The kVCT data were preprocessed by creating a secondary voxel grid at 5 x in-plane resolution of the CT

scan, and assigning the secondary grid voxels that overlapped the contour vertices to the contour structures, which is defined as the 3D voxelized volume described by the contour points. These voxels were termed vertex voxels.

(2) Voxels that lay between consecutive vertex voxels were assigned to the contour structure using Bresenham's algorithm,[22] with the additional constraint that neighboring assigned voxel pairs shared either the same x or y value. Figure 1(a) depicts a 2D slice representation with two vertex voxels, referred to as S and T. Figure 1(b) depicts the voxel assignments connecting S and T using the original Bresenham's algorithm and Fig. 1(c) depicts the voxel assignments with the additional constraint. This process was repeated for all vertex voxels, leading to a series of assigned voxels that formed a closed boundary. The assigned voxels were termed boundary voxels.

(3) The voxels inside the contour boundary voxels were determined and assigned using a GPU based algorithm:
   a. The secondary voxel grid was imported to 3D texture memory.
   b. For each unassigned voxel, an accumulator value was created and initialized to 0.
   c. Parallel rays along the eight cardinal and ordinal directions were passed through each axial plane of the 3D texture.
   d. Each ray sampled every voxel it intersected and updated the voxel's accumulator value. When the ray encountered its first boundary voxel, it added 1 or 2 to every subsequent unassigned voxel's accumulator it intersected, for ordinal or cardinal rays, respectively. The process continued until the ray encountered a second boundary voxel (of any contour). At that point, it stopped adding to the accumulator. As the ray met subsequent boundary voxels, the accumulation process repeated until the ray exited the volume.
   e. Once all rays were traversed, the accumulator dataset was analyzed, and voxels with an accumulator value of 11 or 12 (the maximum) were considered part of the contoured structure.

Figures 1(b) and 1(c) exhibit the ray intersection with the dataset and illustrate the requirement of the modification to Bresenham's algorithm. While the cardinal rays pass through the boundary voxel initiating the accumulation process, the ordinal rays do not intersect with the boundary and may lead to errors. Figure 1(c) depicts the ordinal rays passing through the contoured boundary, illustrating the utility of the structured volume generation algorithm presented above.

(4) Finally, the dataset was downsampled to the original CT resolution, and voxels with greater than 50% of their volume within the contour were considered to be entirely within the contour.

2.C. Mass element generation

The next step in the biomechanical model generation was to initialize the biomechanical model's anatomy. We defined the biomechanical model as consisting of a series of connected mass elements with associated mass–spring damping (MSD) connections in a deformation space where it could be deformed and manipulated. Mass elements were generated at the center of each voxel within the structured volume. For an accurate mass element assignment to specific structures, we ensured the following two constraints: (a) Each contour set included a body contour that covered the entire head and neck anatomy, ensuring that no mass element inside the body was excluded from being assigned to a contour structure and (b) no two contour structures overlapped with each other, ensuring that no ambiguity existed in the mass element assignment process. Each of the mass elements was then associated with a Young's modulus and a Poisson's ratio based on the anatomy as previously tabulated for parotid glands[23] and other structures.[24] In addition, the damping coefficient for each of the mass elements was set to 0.43.[25,26]

2.D. MSD connection initialization algorithm

Connecting the mass elements with each other using a spring damper formulation ensured that the mass elements could deform in a physically realistic manner. To achieve this, the deformation space was first subdivided into a 3D

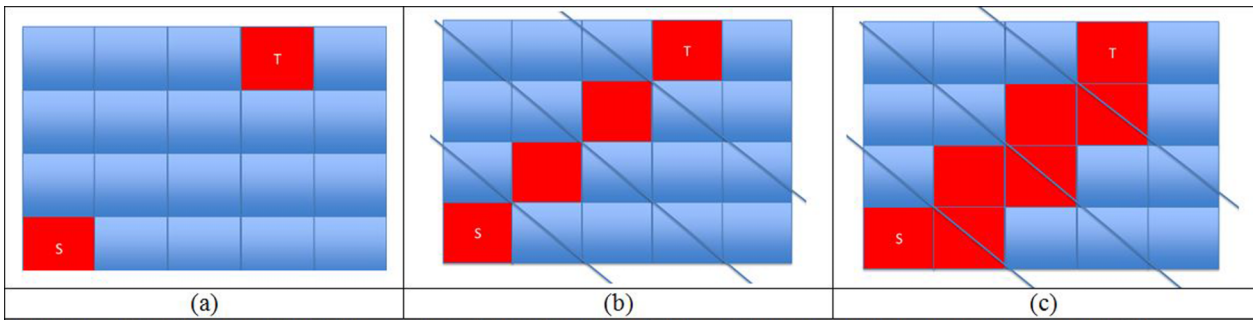

FIG. 1. A schematic description of the contour-filling algorithm. (a) depicts two contour boundary points S and T, (b) illustrates connecting the boundary points using a Bresenham's line generating algorithm, and (c) illustrates connecting the boundary points using the proposed algorithm. The ordinal rays passing through the contour without intersecting the boundary points are illustrated in (b), while the ordinal rays passing through the contour intersecting the boundary points are illustrated in (c).

uniform cell grid, and each mass element was assigned a hash value (or an identification value) based on the cell that contained it. Mass elements were then sorted by their hash value using a GPU based fast radix algorithm.[27] Once sorted, a local neighborhood search was performed in a parallelized manner around each mass element (hereafter referred to as the search element in this section), to find nearby mass elements. When a nearby mass element was within a threshold distance (determined by the voxel size of the input CT) from the search element, a MSD connection was established and the nearby mass element became a connected element for the given search element. The steps in this process were as follows: First, an array in the GPU memory was initialized to hold mass element identifiers for the connected elements of each search element. A second array was initialized in the GPU memory to hold rest state orientations for each of the connections, where the rest state orientation was defined as the vector from the search element to the connected element. At the end of this step, the biomechanical model was complete.

3. COMPUTING MODEL DEFORMATIONS

We defined the head and neck deformation to be actuated by user-defined rigid transformations of skeletal structures. While the skeletal structures underwent rigid transformations, the muscles and the soft tissues in the head and neck region underwent elastic deformations governed by internal corrective forces. The internal corrective forces on each mass element were calculated as a summation of tensile spring force, shear spring force, and a dashpot damping force. At rest state, the elastic internal corrective forces were set to 0. When deformed (as further discussed in Sec. 4), the model's mass elements were relocated to new positions inside the deformation space, which caused the internal corrective forces to be nonzero.

The calculation of the internal corrective forces began by computing the tensile spring force, $\vec{f}_{Y,ab}$, between mass elements a and b[28,29]

$$\vec{f}_{Y,b} = \frac{Y_a + Y_b}{2}\left(\frac{|\vec{p}_{ab}| - |\vec{l}_{ab}|}{|\vec{l}_{ab}|}\right)\frac{\vec{p}_{ab}}{|\vec{p}_{ab}|}, \tag{1}$$

where Y_a and Y_b were the elastic moduli for mass elements a and b, respectively, $\vec{l}_{ab}$ was the rest length orientation for MSD connection between mass elements a and b, and $\vec{p}_{ab}$ was the projection

$$\vec{p}_{ab} = \frac{\vec{l}_{ab}}{|\vec{l}_{ab}|}\left(\frac{\vec{l}_{ab}\cdot\vec{l}'_{ab}}{|\vec{l}_{ab}|}\right), \tag{2}$$

where $\vec{l}'_{ab}$ was the vector from mass element a to mass element b in the deformed state.

The shear spring force, $\vec{f}_{S,ab}$, on mass element a due to mass element b applied along a rejection vector, $\vec{r}_{ab}$, was

$$\vec{f}_{S,ab} = -\frac{S_a + S_b}{2}\left(\frac{\vec{r}_{ab}}{|\vec{l}_{ab}|}\right), \tag{3}$$

where S_a and S_b were the shear moduli for mass elements a and b, respectively, and

$$\vec{r}_{ab} + \vec{l}'_{ab} - \vec{p}_{ab}. \tag{4}$$

The dashpot damping force, $\vec{f}_{v,ab}$, was calculated from the relative velocities of the mass elements, $\vec{v}_a$ and $\vec{v}_b$, and a local damping factor μ_{ab}

$$\vec{f}_{v,ab} = \mu_{ab}(\vec{v}_b - \vec{v}_a). \tag{5}$$

The internal corrective force, $\vec{f}_a$, on mass element a was then computed by summing over all its spring connections

$$\vec{f}_a = \sum_b (\vec{f}_{Y,b} + \vec{f}_{S,b} + \vec{f}_{v,b}). \tag{6}$$

Once the internal forces were computed, the new positions, $\vec{x}_a^{n+1}$, and velocities, $\vec{v}_a^{n+1}$, of the mass elements were updated from the values $(\vec{x}_a^{n}, \vec{v}_a^{n})$ at the previous iteration n, using implicit (backward) Euler integration[30]

$$\vec{v}_a^{n+1} = \vec{v}_a^{n} + \left(\frac{\vec{f}_a}{m_a} + \vec{g}\right)\delta, \tag{7}$$

$$\vec{x}_a^{n+1} = \vec{x}_a^{n} + \vec{v}_a^{n+1}\delta, \tag{8}$$

where δ was the time step between iterations, m_a was the mass of mass element a, and $\vec{g}$ was acceleration due to gravity.

4. MODEL ACTUATION

The next step was actuating the biomechanical head and neck model to represent posture and physiological changes.

4.A. Simulating posture changes

Simulating posture changes was conducted using a three-step model actuation procedure. In the first step, we transformed the 3D skeletal anatomy using a graphical user interface that controlled the individual contoured skeletal structures such as the skull, mandible, and cervical vertebrae. The muscle and the soft tissues were deformed in the second and third steps by applying the soft tissue corrective forces as previously discussed in Sec. 3. During this transformation, the skeletal rotations were constrained at any step to be not more than 1° about a single axis to ensure that the soft tissue deformations occurred in small steps. From a computational perspective, such small soft tissue deformations avoided instabilities that arose from time integration computations.[31,32] Each of the contoured muscle structures was deformed with the skeletal and other soft tissue positions as rigid-body constraints. Similarly, the remaining soft tissue deformations outside any contoured structures were computed with the muscle deformation and skeletal transformations being taken as rigid-body constraints. The deformation process was repeated until all soft tissue structures reached equilibrium deformations.

4.B. Simulating physiological changes

Physiological changes were incorporated on a 3D structured volume basis using a two-step iterative approach. For illustration purposes, we present a scenario where a planning target volume (PTV) underwent regression with all other structure volumes undergoing normal elastic deformations. In the first step, the PTV regression was computed with its surrounding structures providing a rigid-body constraint. For a given change in the PTV volume, the surface area of the PTV volume was reduced in a physically accurate manner by decreasing the rest length of each connection inside the PTV. It was performed as follows: Before a volume change was initiated inside the PTV, its mass elements were clustered to form a set of cuboids. The volume of the set of cuboids was summed to represent the PTV volume.

Using the initial cuboid volume V_i and the volume change v_i for a cuboid i, the change in rest length a_i was computed using

$$(l+a_i)*(w+a_i)*(h+a_i)=V_i+v_i, \tag{9}$$

where l, w, and h were the length, width, and height of each cuboid. From a physiological perspective, the rest length change a_i demonstrated the loss or gain in volume. In order to maintain a stable deformation, the rest length change was constrained to be not greater than 2 mm per iteration. The change in the rest length led to internal elastic corrective forces that subsequently deformed the PTV to reflect the volume regression.

In the second step, the reduced PTV was considered as a rigid body constraint and the remaining soft tissue anatomy surrounding the PTV was deformed as previously explained in Sec. 3. The two-step iterative process continued until the entire anatomy deformation converged.

5. GENERATING KVCT IMAGES REPRESENTING THE DEFORMED ANATOMY

Due to the deformed anatomy, there was not a one-to-one correspondence between mass elements and image voxels. This led to the following issues: (a) gap artifacts where voxels enclosed no mass elements but had a transiting MSD connections, (b) hole artifacts, and (c) aliasing artifacts arising from skeletal head and neck rotations. These three issues were addressed by using the following steps:

(1) A new data volume was initialized that represented the synthetic CT image of the biomechanical model in the deformed state. The data volume dimensions and resolutions were set to be the same as that of the reference kVCT image.
(2) For every mass element in the biomechanical model, the current position was converted from the deformation space into a voxel address in the new data volume.
(3) Each of the new voxels was assigned the Hounsfield intensity (HU) originally associated with the enclosed mass element, or the average HU of multiple enclosed elements.
(4) To address the hole/gap artifacts:
   (a) Ray-traces were defined between every mass element along MSD connections, with interval sampling equal to half of the MSD connection's rest length.
   (b) For every mid-MSD sampled position in the deformation space, the corresponding position in the new data volume was evaluated to see if it was in an empty voxel.
   (c) When the mid-MSD sampled position was in an empty voxel, the HU value was interpolated from the two mass elements connected by the MSD connection with the interpolation weighted by their relative distances from the sample position.
   (d) If one of the mass elements was skeletal anatomy, its corresponding weight was set to 0 to ensure the new data volume maintained the same rigid skeletal structure shape as that of the reference kVCT.
(5) To reduce the aliasing artifacts that occurred during head rotation, we employed a GPU based linear intensity smoothing technique.[33] The method worked as follows:
   (a) The new data volume holding the synthetic CT anatomy was loaded into the GPU's texture memory and sampled at twice its current resolution.
   (b) The trilinear intensity smoothing was then applied on the upsampled data to remove the aliasing artifacts. The intrinsic interpolation removed the artifacts from the feature edges.
   (c) This interpolated image was then downsampled to the original dimensions to produce the final synthetic CT.

6. RESULTS

We now present our results on the model development from a reference head and neck kVCT anatomy and its associated contoured structures. The structure volume generation algorithm presented in Sec. 2.B precisely associated the head and neck voxels to their corresponding contoured structures.

Figure 2(a) shows a planar set of disconnected contour points associated with internal and external boundaries. Figure 2(b) shows the connected contour boundary generated from the planar contour points. The algorithm was able to form nested and distinct boundaries. Figure 2(c) shows the final structure volume with voxels associated with the structure represented in white colored pixels. It can also be seen that the structure volume generation algorithm accurately distinguished the structures inside the inner-most circular boundary to not belong to the contoured structure volume and not associate them with the structure.

Figures 3(a)–3(c) illustrate the head and neck model developed from the reference kVCT. Figure 3(a) shows the rest state of the biomechanical model. The rigid skeletal anatomy can be seen in Fig. 3(c) while the deformable soft tissues are shown surrounding the skeletal anatomy in Fig. 3(a). The volumetric nature of the biomechanical model is shown in

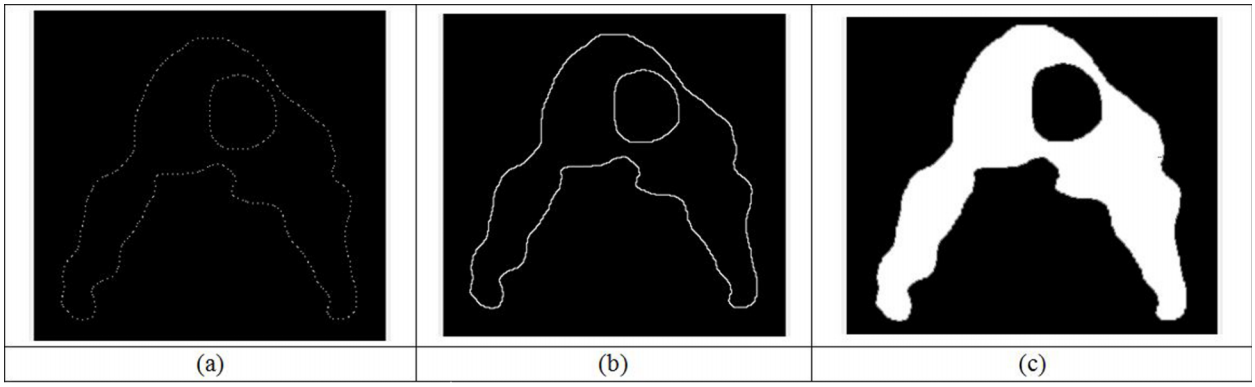

FIG. 2. Contour-filling algorithm. (a) A slice of contour points obtained from a DICOM RT structure. The contour lines that connect all contour points are shown in (b). (c) The volume filled contour structure.

Fig. 3(b) using a 2D slice of the 3D deformable model anatomy that included the contour filled PTV elements and the bone anatomy. The parotid glands are shown on either side of the PTV. The structure volume generation also enables selecting structures undergoing deformation and coupling them with the bone anatomy. Figure 3(c) shows the critical contoured structures along with the skeletal anatomy.

Figures 4(a)–4(c) show the biomechanical deformation caused by skull and neck discs rotation along the caudal–cranial axis. During manipulation of the anatomy, the user has the option to display a color-coded local strain to represent contraction (blue-purple) and expansion (yellow-red) as quantitated in Table I. In this display mode, the soft tissue regions that underwent neither a contraction nor a stretch were colored green. Deformation differences showed the subtle soft tissue and muscle deformations caused by changes in the patient posture during radiotherapy treatment. They also showed the model's fidelity in representing the 3D deformations that a head and neck anatomy undergoes during different postures. Nevertheless, a visual evaluation of the deformations observed for each of the postures also suggested the qualitative accuracy of the observed deformations.

Three examples of the deformation associated with head and neck posture changes are presented in Fig. 5. Figures 5(a)–5(c) show the deformation of a biomechanical model consisting of the head and neck skeletal structure and a PTV, parotid glands, and neck muscles [Fig. 3(c)]. Other muscle structures were excluded for this simulation. The biomechanical deformation of the critical structures, in this case, was caused by skull and cervical vertebrae rotation along the body axis. The strains associated with each of the mass elements are color-coded as previously discussed in Table I. The strains signified a local stretch and contraction that occurred during such skull rotations representing posture changes. The differences in the deformation also showed the muscle deformations caused by changes in the patient posture.

We now present the model results for simulating physiological regression using the reference biomechanical model [shown in Fig. 3(a)]. The PTV was shrunk by 30% to simulate tumor regression. The local distribution of the regression is shown in Fig. 6(a), illustrating the local variations in the tissue expansion and contraction. Figure 6(b) shows the head and neck deformation when the head and neck skeletal structure was rotated by an angle of 10°, both local tissue stretching and tissue compression can be seen during head and neck rotation with simulated PTV regression.

Figures 7(a)–7(c) show a slice of the biomechanical model in the neck region with the PTV. Figures 7(d)–7(f) show the

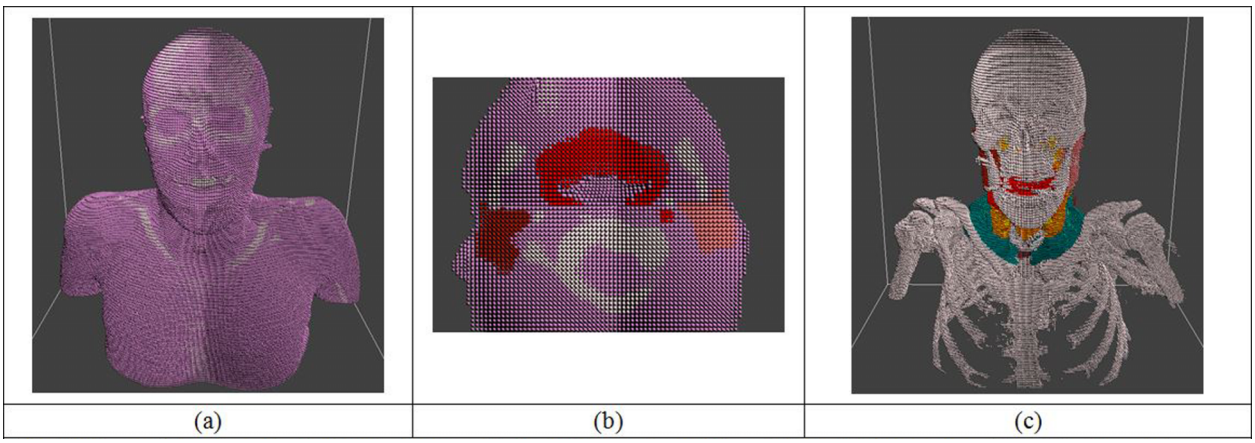

FIG. 3. The model in its rest position is shown with the entire anatomy (a) and the critical contours (c). A 2D slice of the neck region showing the PTV (centrally located), the left and right parotid glands, and the rigid bony structures with surrounding soft tissue is illustrated in (b).

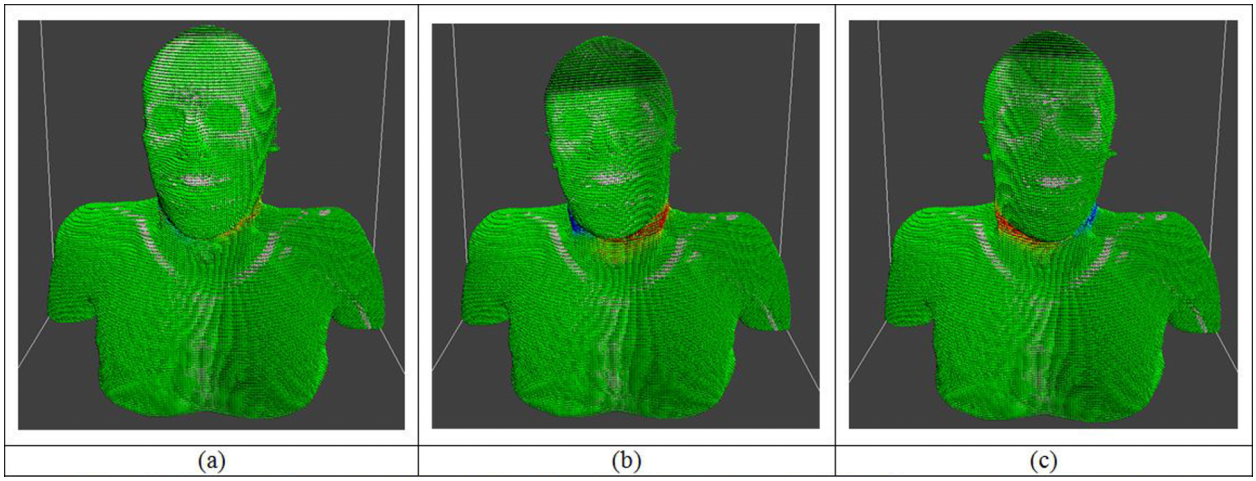

FIG. 4. Biomechanical head and neck deformation with all anatomical substructures. The model before the deformation is shown in (a). Two different neck rotations are demonstrated in (b) and (c).

corresponding stress in the muscle when compared to the original anatomy state. Figure 7(b) shows the internal model changes caused by simulating a PTV shrinkage of 10%. The corresponding deformation strain is shown in Fig. 7(e). Similarly, Fig. 7(c) shows the internal model changes caused by simulating a PTV shrinkage of 30% with the corresponding deformation strain shown in Fig. 7(f). A significant amount of deformation outside the PTV can be observed for each of the cases signifying the role of biomechanical head and neck model. The local distribution of the regression demonstrated the local variations in the tissue expansion and contraction for known PTV regression.

Figure 8 illustrates how the artifacts are compensated for during generation of the simulated kVCT images. The source CT used to generate the model is shown in Fig. 8(a). After a 45° rotation, the hole artifacts are abundant in Fig. 8(b). Fig. 8(c) shows an image after ray-tracing is used to fill the holes, but jagged edges are still apparent. The texture based smoothing algorithm is applied in Fig. 8(d) to produce the final simulated kVCT data set.

Simulated kVCT images corresponding to different states of deformation and rotation are as shown in Figs. 11(a)–11(d). Specifically, Fig. 9(a) shows the 2D slice generated from the model at rest state. The corresponding slice with 30% PTV regression is as shown in Fig. 9(c). The underlying nonrigid deformation of the anatomy during the neck rotation is evident in Fig. 9(b) with no PTV regression and Fig. 9(d) with 30% PTV regression. The differences in the deformations stemmed from changes in the PTV region. Such deformations can only be simulated using a high-resolution physics-based deformation model, which is a key contribution of the paper.

TABLE I. This table documents the normalized color-coding scheme used for representing the strain. R, G, and B represent the red, green, and blue color channels.

Displacement (mm)	R	G	B
−9.9	0.0	0.0	1.0
−6.6	0.0	0.5	1.0
−3.3	0.0	1.0	1.0
0	0.0	1.0	0.0
3.3	1.0	1.0	0.0
6.6	1.0	0.5	0.0
9.9	1.0	0.0	0.0

7. MODEL VALIDATION

In order to validate the numerical accuracy of the biomechanical model, first the general deformation mechanics were tested by comparing the soft tissue response to local global loads with analytic ground-truth calculations. Next, the head and neck models were validated by inducing clinical posture changes in the bony anatomy and comparing the soft tissue deformations induced in the model with the deformations recorded in the clinical data. Finally, the effect of tumor regression was validated by applying a clinically observed deformation to the tumor and comparing the soft tissue deformations induced in the model with the clinical data.

7.A. Soft tissue response to local and global loads

The local load simulation examined the model deformations by applying a known amount of force using a 5 cm radius rigid sphere onto a $10 \times 10 \times 10$ cm^3 cubic piece of tissue and determining the subsequent deformation using the model. The ground-truth deformation was computed using a classical Euler beam theory, which is a simplified method of calculating deflection due to a load using the linear theory of elasticity[34] The two deformations were compared along the row of soft tissue voxels that lay on the cube surface and intersected the contact point between the sphere and the cube. The deformation computed using the proposed system matched the ground truth with a R^2 fit value of >0.98, as shown in Fig. 10(a).

The global load simulation dealt with scenarios where the entire soft tissue structure was applied with a uniform load (e.g., gravity).[34] In the first of two scenarios, the top layer of the soft tissue was anchored and a gravitational force was applied. The resulting deformation was compared with the

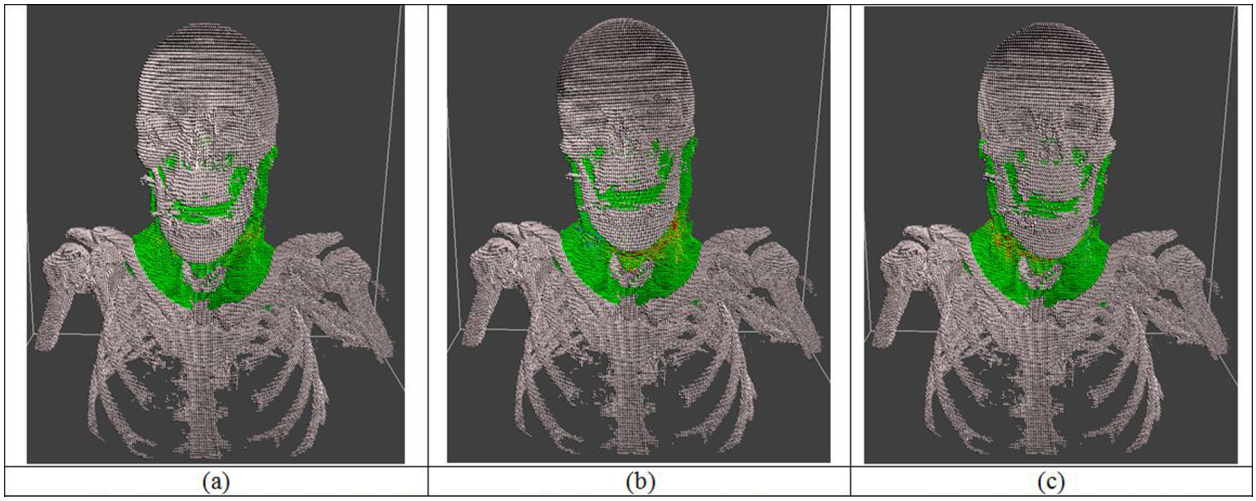

FIG. 5. Biomechanical head and neck deformation with only radiation sensitive structures in the head and neck region. The model before the deformation is shown in (a). Two different head and neck rotations are demonstrated in (b) and (c).

numerical solution provided by Barber.[34] In the second scenario, the direction of gravity was reversed, which led to tissue compression. The model predicted deformation matched well with the ground truth with a $R^2 > 0.98$ for both scenarios, the results of the hanging mass are shown in Fig. 10(b).

7.B. Reproducing clinical deformations

For the purpose of producing ground-truth data to be used for DIR validation in head and neck radiotherapy, the biomechanical model needed to be able to reliably reproduce the type of deformations typically seen in the clinic. To validate the model's ability to do this, ten patients were selected that had weekly kVCT scans over the course of their radiotherapy treatment. An image registration was performed between the initial planning kVCT and a kVCT acquired during the final week of the patient's treatment to obtain the changes in the skeletal positions in the head and neck region. A biomechanical model was assembled from the initial planning CT, and the deformation vectors obtained from the DIR for the skeletal anatomy were applied to the model's skeletal anatomy. This forced the model into the posture of the final week's kVCT, while allowing the soft tissue to deform in response to the changes in skeletal anatomy. An image-based analysis was then performed comparing the planning CT, the final weekly kVCT, and the model generated kVCT equivalent.

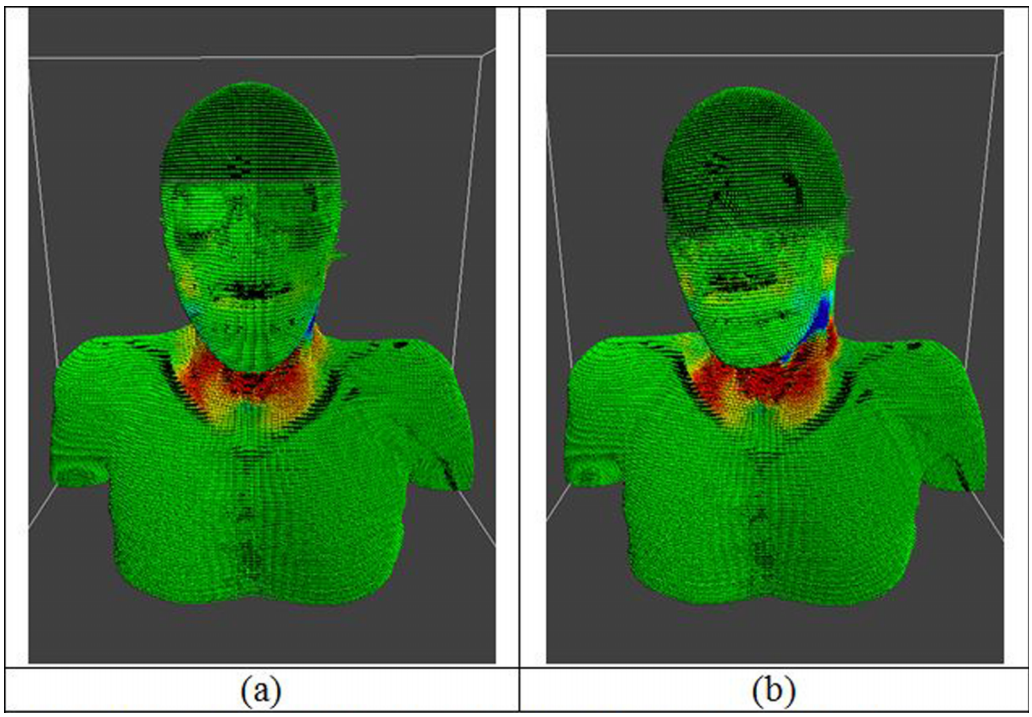

FIG. 6. Biomechanical head and neck deformation with only radiation sensitive structures in the head and neck region. The model before the posture change is shown in (a). A different head and neck posture is demonstrated in (b).

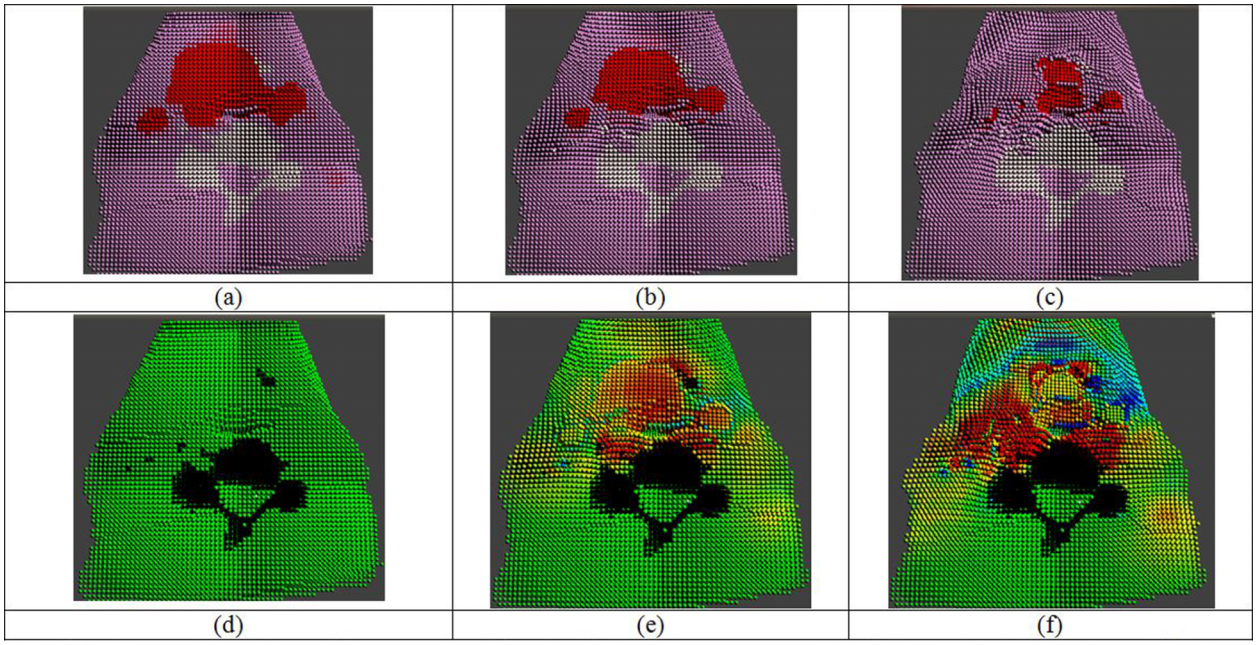

FIG. 7. A 2D snapshot of the model at rest state (a) and its deformed state representing 10% and 40% PTV volume reduction is shown in (b) and (c), respectively. The corresponding strain maps for the three states are shown in (d), (e), and (f).

The Pearson product-moment correlation coefficient[35] was used as the image metric for this analysis. Equation (10) shows the correlation coefficient, with X_i and Y_i representing a voxel intensity of the ground truth (final week's kVCT) and test data (model generated kVCT) sets, while $\overline{X}$ and $\overline{Y}$ represent the mean intensity of the corresponding data sets

$$r = \frac{\sum_{i=1}^{n}\left(X_i-\overline{X}\right)\left(Y_i-\overline{Y}\right)}{\sqrt{\sum_{i=1}^{n}\left(X_i-\overline{X}\right)^2\sum_{i=1}^{n}\left(Y_i-\overline{Y}\right)^2}}. \quad (10)$$

To establish the baseline correlation, the planning kVCT was first correlated with the final weekly kVCT. Analysis was performed on each contoured structure, as well as the entire head and neck region. The results for the primary tumor target, left and right parotids, the spinal cord, and the body are shown in Fig. 11(a) for each of the ten patients. The correlation varies greatly from patient to patient, as the standard deviation for the average correlation of a structure approached 20%. For patient 1, the tumor and right parotid had correlations below 0.5.

The correlation between the model generated data set and the final weekly CT is shown in Fig. 11(b). The displacement of soft tissue voxels ranged from 9.3 to 24.3 mm, with an average maximum of 15.3 ± 4.9 mm. The correlation increased significantly in all cases. The average correlation of the tumor increased from 0.844 ± 0.136 to 0.934 ± 0.017.

This experiment, however, does not allow for physiological changes such as tumor regression. The tumor targets for these patients reduced in volume by an average of 5.1 ± 3.6 mL, with the largest regression in patient 5 at 9.26 mL. The volume changes also induced a shift in the tumor center of mass. The maximum shift was in patient 1 at 15.9 mm, while the average displacement of the center of mass in all ten patients was 4.44 mm. To validate the model's response to tumor regression, the deformation vectors from the DIR were also applied to the primary tumor target as well as the posture changes to the skeletal anatomy. The correlation between the

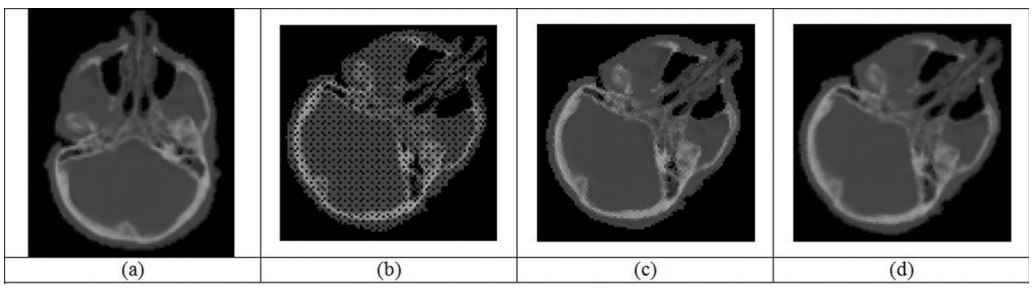

FIG. 8. Simulated kVCT generation and artifact correction. An axial slice of the source kVCT used to generate the model is displayed in (a). After rotating the head by 45°, the resultant model generated image is full of holes and aliasing as shown in (b). Holes are addressed by ray-tracing between model elements and filling holes with an interpolated intensity (c). Aliasing is addressed using a texture based smoothing algorithm to produce the final image (d).

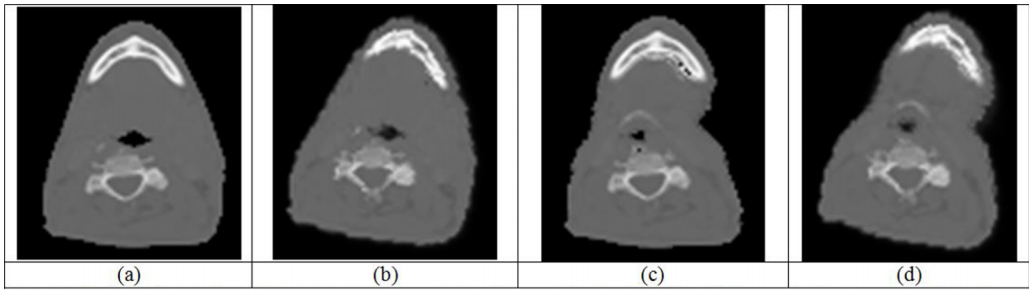

FIG. 9. The kVCT slice at rest state (a) and at a state where the neck is rotated by 10° (b) is shown. The kVCT slice representing the same anatomy with the PTV reduced by 30% is shown in (c). The deformation of the model where the skull is rotated by 10° is shown in (d).

model generated data with tumor regression and the weekly CT is shown in Fig. 11(c). The average correlation coefficient increased from the previous case where only posture changes were introduced. The correlation of the primary tumor target increased to 0.960 ± 0.022.

The model was able to very closely reproduce the soft tissue anatomy seen in a spectrum of clinical patients when posture changes were induced, as seen in Fig. 12. When tumor regression was also set to match the clinical data, the correlation increased even further, such that the lowest correlation of the structures analyzed was still greater than 0.9. This experiment illustrated that the model is capable of simulating physics-based deformations that are very close to clinically seen deformations, and validated the model's ability to ultimately generate ground-truth deformations to be used for DIR validation studies.

8. DISCUSSION

DIR plays a pivotal role in the head and neck adaptive radiotherapy but validation of various DIR algorithms has been hampered by the lack of a quantitative high-resolution ground truth. In this paper, we presented a GPU based high-resolution biomechanical head and neck model using kVCT images that can be used to overcome this difficulty. The biomechanical model will be used for generating CT equivalent 3D volumes that simulate posture changes and physiological regression in order to validate image-guided patient positioning approaches, for example, DIR accuracy of different registration paradigms. The model can also be generated using other volumetric imaging modalities, such as megavoltage CT (MVCT) and cone beam CT (CBCT). Moreover, with the advent of magnetic resonance imaging for both patient simulation and onboard imaging, the model will be an effective tool for generating deformed MRI images and verifying registration accuracy.

It has been previously established that head and neck anatomy involves a complex musculoskeletal feedback system. In this paper, we specifically focus on deforming the muscle and soft tissue system based on known skeletal positions and orientations. The model actuation effectively simulates head and neck deformation from patient posture and physiological regression. The model is currently actuated using a simple graphical user interface that individually controls the skeletal structures in the head and neck region. Such a framework enables us to model soft tissue and muscle deformations representing posture changes. There are multiple methods for introducing anisotropic volume regression. Two simple implementations for the model presented in this paper are adding multiple contours inside a single anatomy and individually controlling the volume regression of the substructures, and

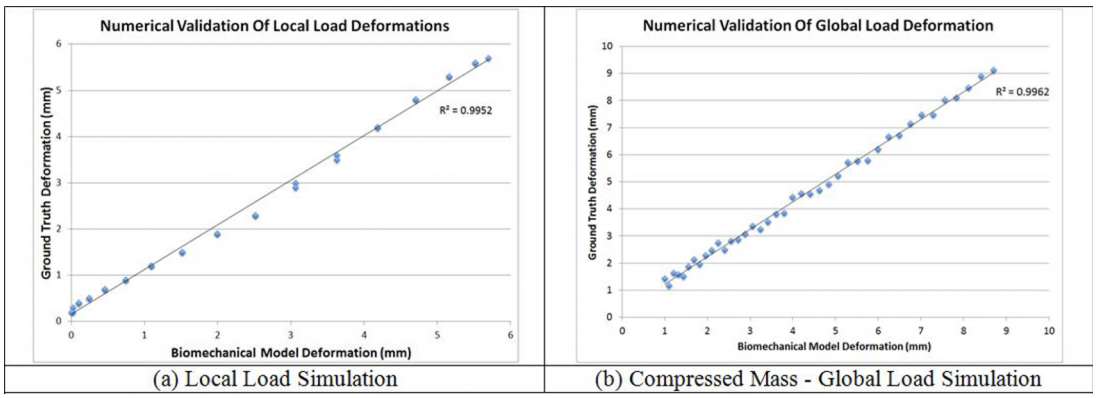

FIG. 10. Elastostatic validation study using local and global force application experiment. A numerical comparison of the elastostatic displacement for a column of voxels is plotted against ground truth computed using a Green's function solution. (a) shows the response of a cube of soft tissue to a local load applied in the form of a spherical mass. (b) shows the response of a cube of soft tissue in response to being compressed by gravity.

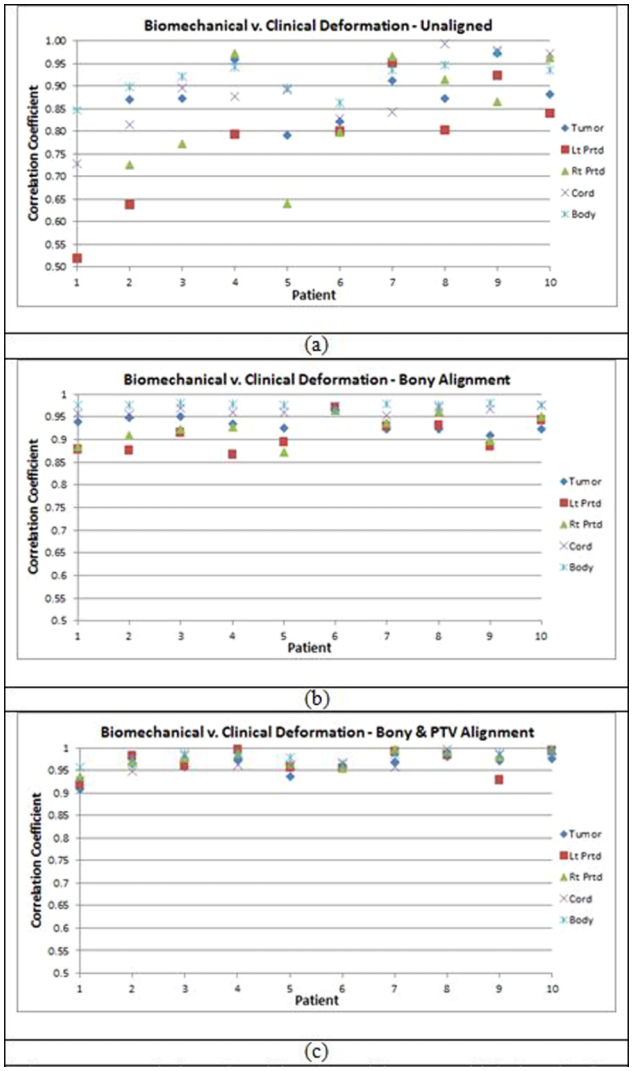

FIG. 11. Correlation of model generated data sets with induced soft tissue deformation from posture changes with clinically observed deformation. (a) shows the baseline correlation between the planning CT used to generate the biomechanical model and the target CT used as the deformation endpoint, (b) shows the correlation after applying posture changes to the model to match the weekly CT, and (c) shows the correlation after the inclusion of tumor regression to the model.

heterogeneously manipulating the elastic properties of the spring connections of an element. To the best of our knowledge, this is the first biomechanical model capable of simulating head and neck physiological changes such as volume regression.

The biomechanical head and neck model discussed in this paper employed a mass–spring approach to deform the head and neck anatomy. While several CPU based mass–spring modeling approaches exist, the model discussed in this paper is unique as it employs a very efficient GPU based approach to deform the head and neck anatomy (discussed in Secs. 4.A and 4.B).

One of the salient features of the biomechanical model is its real-time ability to deform. Using state-of-art graphics processing units, it was observed that the model was able to deform at a rate of 60 deformations per second. While the real-time nature of the model may not have a direct impact on the DIR validation, we envision that it will have a significant impact for online adaptive radiotherapy where DIR plays a key role. Recent advancements in image segmentation, registration, and online adaptive planning have led to systems that can perform their tasks in real-time. Thus having a biomechanical model guided validation that can match the speed provided by these algorithms will also be essential for future developments in adaptive radiotherapy.

Future work will focus on improving the skeletal model to simulate more physically and physiologically realistic articulation. The biomechanical properties in our model were obtained from the literature, but these properties vary between patients. We will develop a technique for estimating patient specific tissue elastic properties by inversing the forward deformation model for known deformations. This will provide patient specific head and neck biomechanical models which will be useful for adaptive radiotherapy. While others have used low resolution finite element models to estimate elastic properties, the proposed high-resolution model with its complex musculoskeletal behavior will provide a more accurate estimation. The GPU based platform presented in this paper enables the complex calculations to be performed in parallel and in a scalable fashion in nearly real-time.

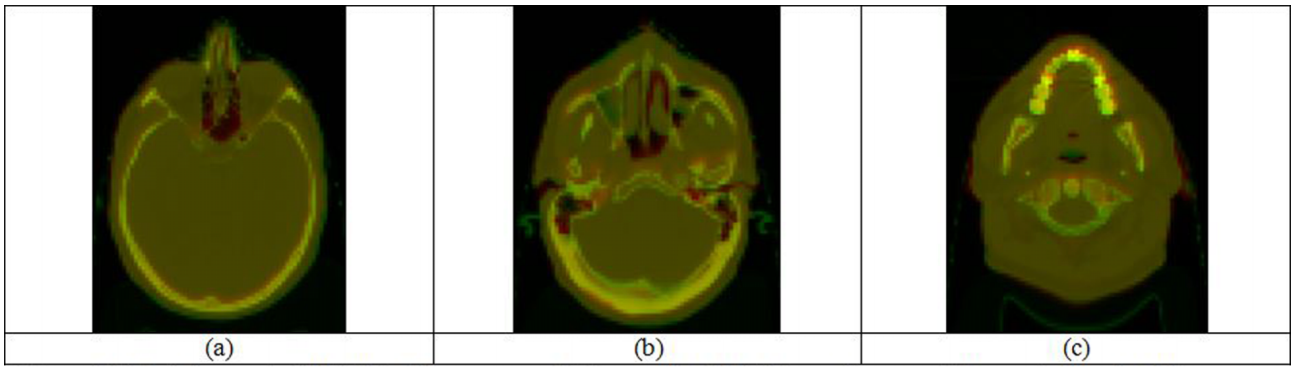

FIG. 12. Model generated kVCT (red) images overlaid on weekly kVCT (green) images at three axial levels. Yellow areas show good agreement between the model generated images and the weekly CT images. Areas tinted more green or red show a disagreement where one image had a higher intensity.

[a]Author to whom correspondence should be addressed. Electronic mail: jneylon@mednet.ucla.edu

[1]Institute, N. C., " NCI fact sheet on head and neck cancer" (available URL: http://www.cancer.gov).
[2]S. M. Bentzen, L. S. Constine, J. O. Deasy, A. Eisbruch, A. Jackson, L. B. Marks, R. K. T. Haken, and E. D. Yorke, "Quantitative analyses of normal tissue effects in the clinic (QUANTEC): An introduction to the scientific issues," Int. J. Radiat. Oncol., Biol., Phys. **76**, S3–S9 (2010).
[3]K. Britton, L. Dong, and R. Mohan, "Image guidance to account for inter-fractional and intrafraction variations: From a clinical and physics perspective," in *Image-Guided Radiotherapy of Lung Cancer*, edited by J. Cox, J. Chang, and R. Komaki (Informa Healthcare, Inc., New York, NY, 2007).
[4]X. A. Li, F. Liu, A. Tai, and E. Ahunbay, "Development of an online adaptive solution to account for inter and intra-fractional variations," Radiother. Oncol. **100**(3), 370–374 (2011).
[5]F. Liu, B. Erickson, C. Peng, and X.A. Li., "Characterization and management of interfractional anatomic changes for pancreatic cancer radiotherapy," Int. J. Radiat. Oncol., Biol., Phys. **83**(3), e423–e429 (2012).
[6]J. Stewart, K. Lim, V. Kelly, and J. Xie, "Automated weekly replanning for intensity-modulated radiotherapy of cervix cancer," Int. J. Radiat. Oncol., Biol., Phys. **78**(2), 350–358 (2010).
[7]A. Bujold, T. Craig, D. Jaffray, and L. Dawson, "Image-guided radiotherapy: Has it influenced patient outcomes?," Semin. Radiat. Oncol. **22**(1), 50–61 (2012).
[8]J. Wang, S. Bai, and N. Chen, "The clinical feasibility and effect of online cone beam computer tomography guided intensity modulated radiotherapy for nasophyrngeal cancer," Radiother. Oncol. **90**, 221–227 (2009).
[9]C. Lee and K. M. Langen, "Assesment of parotid gland dose changes during head and neck cancer radiotherapy using daily megavoltage computed tomography and deformable image registration," Int. J. Radiat. Oncol., Biol., Phys. **71**(5), 1563–1571 (2008).
[10]A. A. Mayah, J. Moseley, S. Hunter, M. Velec, L. Chau, S. Breen, and K. Brock, "Biomechanically-based image registration of head and neck radiation treatment," Phys. Med. Biol. **55**, 6491–6500 (2010).
[11]K. Kahler, J. Haber, H. Yamauchi, and H. Seidel, "Head shop: Generating animated head models with anatomical structure," in *Proceedings of the 2002 ACM SIGGRAPH/Eurographics Symposium on Computer Animation* (ACM, New York, NY, 2002), pp. 55–64.
[12]E. Sifakis, I. Neverov, and R. Fedkiw, "Automatic determination of facial muscle activations from sparse motion capture marker data," ACM Trans. Graphics **24**(3), 417–425 (2005).
[13]S. H. Lee and D. Terzopoulos, "Heads up! biomechanical modeling and neuromuscular control of the neck," ACM Trans. Graphics **25**(3), 1188–1198 (2006).
[14]V. B. Zordan, B. Celly, B. Chiu, and P. C. Dilorenzo, "Breathe easy: Model and control of simulated respiration for animation," in *Proceedings of the 2004 ACM SIGGRAPH/Eurographics Symposium on Computer Animation* (Eurographics Association, Aire-la-Ville, 2004), pp. 29–37.
[15]M. Harders, R. Hutter, A. Rutz, P. Niedere, and G. Szekely, "Comparing a simplified FEM approach with the mass–spring model for surgery simulation," Stud. Health Technol. Inf. **94**, 109 (2003).
[16]P. C. Dilorenzo, V. B. Zordan, and B. L. Sanders, "Laughing out loud: Control for modeling anatomically inspired laughter using audio," ACM Trans. Graphics **27**(5), 1–8 (2008).
[17]I. Albrecht, J. Haber, and H. Seidel, "Construction and animation of anatomically based human hand models," in *Proceedings of the 2003 ACM SIGGRAPH/Eurographics Symposium on Computer Animation* (Eurographics Association, Aire-la-Ville, 2003), pp. 98–109.
[18]W. Tsang, K. Singh, and E. Fiume, "Helping hand: An anatomically accurate inverse dynamics solution for unconstrained hand motion," in *Proceedings of the 2005 ACM SIGGRAPH/Eurographics Symposium on Computer Animation* (ACM, New York, NY, 2005), pp. 319–328.
[19]A. Santhanam, T. Willoughby, A. Shah, S. L. Meeks, J. Rolland, and P. Kupelian, "Real-time simulation of 4D lung tumor radiotherapy using a breathing model," Lect. Notes Comput. Sci. **5242**, 710–717 (2008).
[20]A. I. Veress, W. P. Segars, J. A. Weiss, B. M. Tsui, and G. T. Gullberg, "Normal and pathological NCAT phantom data based on physiological realistic left ventricle finite element models," IEEE Trans. Med. Imaging **25**(12), 1604–1616 (2006).
[21]T. Komura, Y. Shinagawa, and T. L. Kunii, "Creating and retargeting motion by the musculoskeletal human body model," Visual Comput. **16**(5), 254–270 (2000).
[22]J. E. Bresenham, "Algorithm for computer control of a digital plotter," IBM Syst. J. **4**(1), 25–30 (1965).
[23]K. Arda, N. Ciledag, E. Aktas, B. Aribas, and K. Köse, "Quantitative assessment of normal soft-tissue elasticity using shear-wave ultrasound elastography," AJR, Am. J. Roentgenol. **197**, 532–536 (2011).
[24]L. Huang, N. Bakker, J. Kim, J. Marston, J. Tis, and D. Cullinane, "A multi-scale finite element model of bruising of soft connective tissue," J. Forensic Biomech. **3**, 1–5 (2012).
[25]H. Shi, *Finite Element Modeling of Soft Tissue Deformation* (University of Louisville, Louisville, KY, 2007).
[26]T. Tilleman, M. Tilleman, and M. Neumann, "The elastic properties of cancerous skin: Poisson's ratio and Young's modulus," Isr. Med. Assoc. J. **6**, 753–755 (2004).
[27]M. Harris, S. Sengupta, and J. D. Owens, "Parallel prefix sums (scan) with CUDA," in *GPU Gems 3* (Addison-Wesley, New York, NY, 2007).
[28]A. Boresi, *Elasticity in Engineering Mechanics*, 3rd ed. (Wiley, New York, NY, 2000).
[29]A. E. H. Love, *A Treatise on Mathematical Theory of Elasticity* (Dover Publications, New York, NY, 2011).
[30]W.-M. Hwu, *GPU Computing Gems Jade Edition*, 1st ed. (Morgan Kaufmann/Elsevier, Burlington, MA, 2012), Vol. 2.
[31]E. Rougier, A. Munjiza, and N. W. M. John, "Numerical comparison of some explicit time integration schemes used in DEM, FEM/DEM and molecular dynamics," Int. J. Numer. Methods Eng. **61**, 856–879 (2004).
[32]J. Mesit, R. Guha, and S. Chaudhry, "3D soft body simulation using mass–spring system with internal pressure force and simplified implicit integration," J. Comput. **2**(8), 34–43 (2007).
[33]C. Sigg and M. Hadwiger, "Fast third-order texture filtering," in *GPU Gems 2*, edited by M. Pharr and R. Fernando (Addison-Wesley Professional, Boston, MA, 2005).
[34]J. R. Barber, *Elasticity, Solid Mechanics and its Applications*, 3rd ed. (Springer, New York, NY, 2009).
[35]J. L. Rodgers, J. L. Nicewander, and W. A. Nicewander, "Thirteen ways to look at the correlation coefficient," Am. Stat. **42**, 59–66 (1995).